^{17}O NMR relaxation measurements for investigation of molecular dynamics in static solids, using sodium nitrate as a model compound

Liliya Vugmeyster, [a] Riqiang Fu, [b] Dmitry Ostrovsky [c]

[a] *Department of Chemistry, University of Colorado Denver, Denver CO USA 80204*

[b] *National High Magnetic Field Laboratory, Tallahassee, FL USA 32310*

[c] *Department of Mathematics, University of Colorado Denver, Denver CO USA 80204*

[a,*]Department of Chemistry, University of Colorado at Denver, 1201 Larimer St, Denver, CO 80204; email: LILIYA.VUGMEYSTER@UCDENVER.EDU

Abstract

^{17}O NMR methods are emerging as a powerful tool for determination of structure and dynamics in materials and biological solids. We present experimental and theoretical frameworks for measurements of ^{17}O NMR relaxation times in static solids focusing on the excitation of the central transition of the ^{17}O spin 5/2 system. We employ ^{17}O-enriched $NaNO_3$ as a model compound, in which the nitrate oxygen atoms undergo 3-fold jumps. Rotating frame ($T_{1\rho}$), transverse (T_2) and longitudinal (T_1) relaxation times as well as line shapes were measured for the central transition in the 280 to 195 K temperature range at 14.1 and 18.8 T field strengths. We conduct experimental and theoretical comparison between different relaxation methods and demonstrate the advantage of combining data from multiple relaxation time and line shape measurements to obtain a more accurate determination of the dynamics as compared to either of the techniques alone. The computational framework for relaxation of spin 5/2 nuclei is developed using the numerical integration of the Liouville – von Newman equation.

Introduction

Advancement in method development of ^{17}O NMR led to significant progress in structural and dynamics studies of materials and biomolecules.[1,2,3,4,5,6,7,8] ^{17}O is spin 5/2 quadrupolar nucleus with a wide range of quadrupolar coupling constant (C_q) values possible, up to tens of MHz. Both first order and second order quadrupolar interaction govern its spin physics, but the central transition (CT), i.e. the transition between the m_z = +1/2 and m_z = –1/2 states, is not affected by the first order contribution. Thus, it yields relatively narrow line shapes and most works have focused on detecting this transition. [2]

^{17}O nuclei are sensitive dynamics probes and distortions in quadrupolar line shapes induced by motions can be used to quantify the motions.[2,9,10,11] In addition, relaxation measurements can provide useful complementary information on the variety of time scales. We are particularly interested in the relaxation in the solid phase due to potential applications of relaxation approaches to a variety of non-soluble compounds, including biomolecular solids. Recent advances in ^{17}O labeling approaches will likely enable numerous future applications of ^{17}O solid state NMR relaxation methods.

The goal of the manuscript is to compare dynamics information from several ^{17}O NMR relaxation times measurements, such as rotating frame ($T_{1\rho}$), transverse (T_2) and longitudinal (T_1) as well as line shapes

analysis and to assess whether the combined approach including all measurements can increase the accuracy of the molecular dynamics information in solids.

Quadrupolar relaxation in the solid state is challenging from both experimental and modeling perspective. For spin 5/2 the base set spans 35 coherences and the relaxation, in general, is inherently non-exponential. [12,13] As a result, the initial conditions can heavily influence the apparent relaxation times, as shown by Haase et al. for longitudinal T_1 relaxation times.[14] Coherent evolution of half-integer quadrupoles under spin-lock has been considered in detail by Wimperis and co-workers.[15,16] Additionally, the laboratories of Verbelow and Veeman has presented an extensive body of work describing the theory of the nutation experiment and relaxation of multiple quantum coherences for half-integer nuclei.[17,18] Approaches based on the numerical simulations of the Liouvillian equation can provide means of parametrizing experimentally observed dynamics. [19]

The model compound used here, ^{17}O-labeled $NaNO_3$, was recently studied in detail by line shapes measurements by Hung and coworkers[9] as well as by Beerwerth et al.[20] The main motions are the 3-fold jumps of the nitrate group. Two motional transitions were seen in this compound, including the one at which the rate of motions matches the second order quadrupolar interaction. The dynamics were analyzed using the full Liouvillian approach by Hung et al. [9] In addition to the quadrupolar interaction, the chemical shift anisotropy(CSA) interaction has to be taken into account.

We first present theoretical consideration of the ^{17}O laboratory and rotating frame relaxation and examples of the 2-site jump simulations (Figure 1A) in solids using the Liouvillian approach. These simulations are performed for an axially symmetric quadrupolar (EFG) tensor with an arbitrary value of the quadrupolar coupling constant of 10 MHz and the jump angle of 104.5°. The theoretical description is followed by the experimental section of the relaxation rates and line shapes measurements in the powder-state of $NaNO_3$. The geometry of the EFG and CSA tensors in $NaNO_3$, the notation for the tensor components as well as their values as determined in reference [9], are illustrated in Figure 1B.

To our knowledge, ^{17}O $T_{1\rho}$ relaxation times measurements have not yet been implemented to studies of molecular dynamics in solids, and we present in detail experimental and simulations approaches for this technique. The simulations protocol to generate ^{17}O NMR laboratory and rotating frame relaxation rates for solids undergoing stochastic jumps is presented and is generalizable in principle to any type of molecular motions in the solid state. Experimental $T_{1\rho}$, T_1, and T_2 times as well as the line shape data are obtained in 280 to 195 K temperature range, and the rate constants of 3-fold jumps are obtained for all series. We then obtain the Arrhenius activation energy from the combined data set.

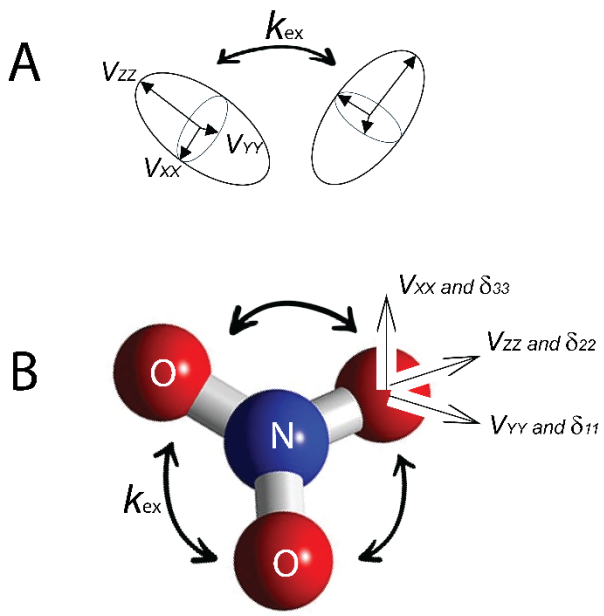

Figure 1. A) A schematic representation of an axially symmetric quadrupolar tensor undergoing a 2-site conformational exchange process with the exchange constant k_{ex}. In the theory section we use the jump angle of 104.5°, $V_{zz} = C_q = 10$ MHz and $\eta = \frac{V_{yy} - V_{xx}}{V_{zz}} = 0$. B) Ball-and-stick representation of the NO_3^- ion, in which the oxygen atoms undergo the 3-fold jumps with the rate constant k_{ex}. The quadrupolar and CSA tensor orientations in their corresponding principal axes systems are shown explicitly, such that their major axes are aligned and pointing along the N-O bond. $V_{zz} = C_q = 12.5$ MHz, $\eta = 0.8$, $[\delta_{11}, \delta_{22}, \delta_{33}] = [250, 400, 550]$ ppm.

Results and Discussion

I. Theoretical and computational description of the ^{17}O NMR relaxation in powders

Hamiltonian description for spin 5/2 system

In the presence of a static magnetic field and a radiofrequency field applied in the transverse plane the Hamiltonian for a single ^{17}O nuclear spin ($I = 5/2$) in a frame rotating with Larmor frequency can be written as

$$H = H_Q + H_{RF} + H_{CS}, \quad (1)$$

where $H_{RF} = \omega_{RF} I_x$ is the spin-locking interaction applied on-resonance and $H_{CS} = \omega_0 \sigma_{zz} I_z$ is the chemical shift interaction. The circular part of the quadrupolar interaction tensor H_Q includes the first and second order terms in the average Hamiltonian perturbation theory

$$H_Q = H_{Q,1} + H_{Q,2}, \quad (2)$$

with the following definitions, using the notation and the choice of tensor definitions given in[21].

$$H_{Q,1} = \frac{eQ}{I(2I-1)\hbar}\sqrt{\frac{3}{8}}[I_z^2 - I(I+1)/3]V_0 \quad (3)$$

$$H_{Q,2} = \frac{1}{\omega_0}\left(\frac{eQ}{I(2I-1)\hbar}\right)^2 I_z\left(\left[I_z^2 - I(I+1)/2 + 1/8\right]V_1V_{-1} + \left[I_z^2 - I(I+1) + 1/2\right]V_2V_{-2}/4\right)$$

ω_0 is the Larmor frequency and V_i are the spherical components of the EFG tensor. The EFG tensor is defined in its principal axis system (PAS) as

$$(V_2,V_1,V_0,V_{-1},V_{-2})^{PAS} = eq(\,1/2\,,0,\sqrt{3/2},0,\,1/2\,)$$

and then transformed to the laboratory frame by Wigner matrices. The overall strength of the first order quadrupolar interaction is given by the quadrupolar constant $C_q = \frac{e^2qQ}{\hbar}$ and, for a particular orientation of the EFG tensor in the laboratory frame, by

$$\omega_q = \frac{3}{4I(2I-1)}\frac{2\pi C_q}{}\left[\frac{3\cos^2\theta - 1}{2} + \frac{\eta}{2}\sin^2\theta\cos 2\varphi\right],$$

where θ and φ are azimuthal and polar angles of the transformations respectively.[13]

Inclusion of the exchange matrix and simulations for large-angle 2-site jumps motions

The coherent spin evolution described by the Hamiltonian of Eq. (1) can be represented in the form of a system of linear differential equations acting on the density matrix ρ of spin *I*. The matrix of such a system is the Liouville operator, *L*. The changing magnetic environment of a spin can be described by the exchange between different orientations of EFG and CSA tensors. They correspond to different orientations of a given molecule within the laboratory frame. Therefore, the spin state of the system can be described by a direct product of density matrices for individual spin states and vectors describing the exchanging molecular orientations. The exchange between different orientations can be represented by a Markovian exchange matrix. We thus arrive at the general form of the Liouville – von Neumann equation for the combined density matrix

$$\frac{d\rho_{i,m}}{dt} = iL_{ij}^{(m)}\rho_{j,m} + K_{mn}\rho_{i,n} \qquad (4)$$

where the indices *i* and *j* refer to the spin degrees of freedom and *m* and *n* to the orientational (spatial) degrees of freedom. The Markov exchange process leads to relaxation. Relaxation included in Eq. (4) are only due to the fluctuations of the secular terms included in the Hamiltonians of Eqs. (2) and (3). The relaxation from terms fluctuating with Larmor and double Larmor frequency will be calculated in the Redfield theory limit[13] and included explicitly into Eq. (4),[22] modifying it to

$$\frac{d\rho_{i,m}}{dt} = iL_{ij}^{(m)}\rho_{j,m} + K_{mn}\rho_{i,n} - R_{ij}(\rho_{j,m} - \rho_{j,m}^0) \qquad (5)$$

where $\rho_{j,m}^0$ indicates the equilibrium coherence.

In general, the density matrix for spin *I* = 5/2 can be represented in the basis of 35 basic coherences. When a particular coherence will be referred to, we will use the rank-order basis $T_p^l(s,a)$, [23] listed in Eq. (S1). Laboratory frame relaxation for half-integer quadrupolar nuclei has been considered in detail in the past and shown to be non-exponential in general, and in particular for powder solids.[12,13,14,24,25,26] There are three coherences involved in the R_1 relaxation. They correspond to three possible absolute values of magnetic number $|m_z|$: the central transition $I_z(CT)$, the first satellite transition $I_z(ST1)$, and the second

satellite transition $I_z(ST2)$. The explicit expressions for these coherences in the $T_p^l(s,a)$ basis are given in Eq. (S3). The longitudinal relaxation processes cause interconversions between these three coherences, creating non-exponential magnetization recovery/build-up curves. For the transverse magnetization with no spin-locking field applied and neglecting the CSA interaction, there are again three coherences corresponding to $|m_z| \leftrightarrow |m_z|-1$ transitions $I_x(CT)$, $I_x(ST1)$, and $I_x(ST2)$ defined in Eq. (S4). The relaxation process is non-exponential as well, due to the interconversions between these coherences.

Though inherently non-exponential, the relaxation decay and build up curves can be phenomenologically treated as nearly exponential in many situations. Precise characterization of nonexponentiality of the relaxation curves is difficult, unless there is a significant contribution from the components which differ in their relaxation rates by a factor of 5 or more. Because the focus of this work is not to study non-exponentiality of the relaxation itself, but to advance the methods of extracting dynamic parameters from relaxation experiments, we fit both experimental and simulated relaxation build up and decay curves with a monoexponential function with a baseline, $M(t) = M_0 e^{-t/T} + B$. The baseline effectively removes contributions of very slowly relaxing components, while T gives a good approximation to the values of T_1, T_2, and $T_{1\rho}$ for the respective experiments. This approximation should not lead to a bias in the fitted exchange rates when relaxation delay times used in simulations and experiments are chosen to be the same.

Rotating frame relaxation

Relaxation of the transverse magnetization in the presence of a spin-lock field is less discussed in the literature and we will focus on it below. We will then compare its key features to the R_1 and R_2 experiments. We will first consider the coherent evolution of the density operator in the absence of any exchange or any other sources of relaxation. As the initial condition we take $\rho(0)$ corresponding to the single quantum transverse magnetization and select the spin-locking RF field strength in the interval $\frac{1}{\omega_0}\left(\frac{2\pi C_q}{I(2I-1)}\right)^2 \ll \omega_{RF} \ll \frac{2\pi C_q}{I(2I-1)}$, such that only the central transition is effectively locked for the majority of the orientations, aside from the case when the polar angle θ matches the magic angle at which the first order quadrupolar interaction vanishes. This is the special case of a more general RF field range considered for the coherent evolution under spin-lock by Wimperis et al.[16]. The quadrupolar interaction induces mixing of the initial $I_x(CT)$ coherence with other basis coherences, including those corresponding to the satellite transitions. The locking efficiency is orientation-dependent because of the variations in the strengths of the first and second order quadrupolar interactions.

Out of the 35 coherences, 20 symmetric coherences (Eq S2) are involved in the evolution during the spin-lock period when the initial coherence is $I_x(CT)$, for the case of the on-resonance spin-locking field and no CSA contribution. Out of these, 5 combinations form eigenvectors of the evolution operator with zero eigenvalue, i.e, these are the "locked" eigenvectors. The exact form of this space of locked coherences in terms of the individual basis coherences depends on the Larmor frequency, the RF field strength, the quadrupolar tensor parameters, as well as on crystallite orientations. In general, there appears to be no easily recognizable pattern among them, unlike in the cases of R_1 and R_2 relaxation. Supporting Information SI 1 provides several illustrative examples.

Figure 2A shows the projection coefficient of single quantum coherence $I_x(CT)$ on the subspace of locked coherences versus the quadrupolar frequency ω_q for a selected set of parameters (an axially symmetric EFG

tensor with $C_q = 10$ MHz, $\eta = 0$, $\omega_0/2\pi = 54.2$ MHz, $\omega_{RF}/2\pi = 35$ kHz) in the absence of motions at $t = \infty$. We also show individual calculations when only the first order or the second order quadrupolar interactions are taken into account. Note that the second order interaction (Q2), which is proportional to ω_q^2/ω_0, reduces the locking efficiency, as noted by Wimperis 2009. [16] Figure 2B shows three other time points in the 10 to 80 μs range to demonstrate the time-dependence of coherent oscillations due to the oscillatory component of $I_x(CT)$ arising as the result of interconversions between other elements of the basis (a total of 20 coherences listed in Eq. S2). Figure S1 shows full time-dependent curves for selected crystallite orientations.

In the absence of motions, the locking efficiency for the case of Figure 2A ranges from about 30% for small ω_q values and reaches up to 100% for large values of ω_q. The low efficiency for small values of ω_q is governed by dephasing due to Q2 term, which is the dominant term for small values of ω_q. On the other hand, for large values of ω_q the Q2 interaction is less efficient than Q1, which induces locking of non-I_x coherences during the spin-lock period.

Figure 2C shows an analogous situation in the presence of large-angle 2-site jumps with equal populations, the jump angle of 104.5° and the rate constant of $1 \cdot 10^5\ s^{-1}$. In the presence of motions, the results are shown for the time points 0.082 and 2.2 ms, corresponding to the apparent bi-exponential fit of the simulated magnetization decay curve (averaged over the powder pattern and shown in Figure S2). The *x*-axis represents the value of ω_q for one of the two exchanging site orientations, while the values of time-evolved $I_x(CT)$ coherence shown on the vertical axis are averaged over all possible orientations of the second site. Crystallites orientation with values of ω_q within the ±20 kHz range were averaged, in order to decrease scatter in the data. Aside from the overall loss of intensity due to relaxation, one can observe a clear broadening of the pattern (Figure 2C blue and red lines, shown for $k_{ex} = 1 \cdot 10^5\ s^{-1}$) compared to the one in the absence of motion (black line), indicative of mixing of the crystallite orientation due to motions. To probe the effect of k_{ex} magnitude on this pattern (Figure 2D), we select the snapshots of the projected $I_x(CT)$ approximately corresponding to the value of $T_{1\rho}$ taken from the fast component (i.e., the initial decay) of magnetization decay curves. The patterns are normalized to the maximum of each curve, which visually de-emphasizes the effect of the reduction in the projected $I_x(CT)$ intensity and displays the distortions in the overall patterns. In the k_{ex} range of 10^2 to $10^6\ s^{-1}$ the patterns are similar, but in the range between 10^7 to $10^{10}\ s^{-1}$ the broadening becomes even more pronounced, such as the distinctions between different crystallites orientation are further blurred. This indicates an intermediate to fast motional regime. One notable exception is the case when one of the exchanging orientations is parallel to the magnetic field (high ω_q limit), for which the distinction remains.

To further define the intermediate regime, we examine rotating frame relaxation rates $R_{1\rho}$ as a function of k_{ex} for two selected initial crystallite orientations, 0 and 90 ° with respect to the magnetic field (Figure 3). The orientations of the exchanging sites, constrained by the 104.5° jump angle, are averaged in the $R_{1\rho}$ rate calculations. A single exponential fit is assumed for this analysis. The $R_{1\rho}$ versus k_{ex} pattern has two maxima, the positions of which are determined roughly by the conditions $k_{ex} = \omega_q$ and $k_{ex} = \omega_0$. Thus, the intermediate motional regime in this case is qualitatively given by the range $\omega_q < k_{ex} < \omega_0$. The dependence on ω_0 is considered in more detail in Figure S3, in which we calculate $R_{1\rho}$ rates for three crystallite orientations for 9.4 T and 5·9.4 T static magnetic field strength. The field-dependence is most

pronounced in the intermediate regime and is also evident in the slow regime. The extent of field dependence varies with the crystallite orientation.

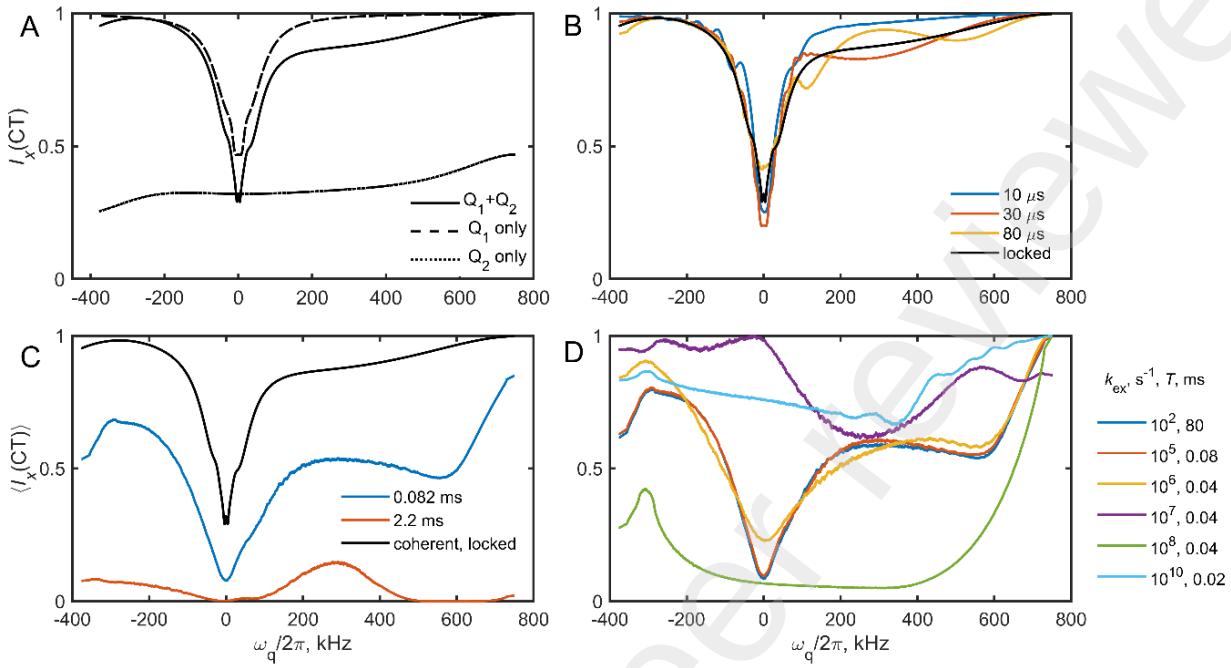

Figure 2. Simulated transverse magnetization $I_x(CT)$, corresponding to the central transition of ^{17}O spin-5/2 system with an axially symmetric EFG tensor with C_q= 10 MHz under the spin-lock field of 35 kHz and 9.4 T magnetic field, as a function of orientation-dependent frequency ω_q under static(non-spinning) conditions. A) The locked component in the absence of motions for both the first and second order quadrupolar interactions Q_1+Q_2 (solid line), or the first order quadrupolar interaction only (dashed line), or the second order quadrupolar interaction only (dotted line). B) After coherent evolution under the full quadrupolar interaction, with the evolution times shown directly on the panel. The black line corresponds to the locked component. C) Including 2-site jumps of the EFG tensor principal axis, using $k_{ex} = 10^5$ s^{-1} and the jump angle of 104.5°, averaged over the azimuthal angle of the second site. Shown for evolution times corresponding to fast (0.082 ms) and slow (2.2 ms) relaxation times of the magnetization decay curve, and averaged over crystallite orientations. The black line corresponds to the locked component of the coherent evolution. D) Including the 2-site jumps as in C) for the k_{ex} and evolution times values shown on the panel. The normalization is performed to the maximum value of $\langle I_x(CT)\rangle$ for each individual curve. The evolution times are chosen to approximate $T_{1\rho}$ times, using the single-exponential fits of the powder-averaged magnetization decay curves. For panels B)-D) the values of $I_x(CT)$, excluding the locked coherent lines, are averaged over the $\pm$ 20 kHz intervals around the values ω_q shown on the *x*-axes, to increase smoothness. Simulations are based on 17711 crystallite orientations.

Similar results are obtained when averaging over the entire powder pattern is considered and are shown in Figure 3B for $C_q = 10$ MHz. In the slow motional regime the field-dependence can be quenched for small C_q values. Figure S4 demonstrates these results for $C_q = 1$ MHz and $\omega_{RF}/2\pi = 3.5$ kHz, with the conditions for the RF field amplitude chosen in such a way as to keep the extent of locking constant.

In the slow limit, the $R_{1\rho}$ relaxation rate is governed by the difference in the percentage of locked $I_x(CT)$ for the exchanging orientations multiplied by k_{ex}. When the time scale of the exchange is slower than the rate of coherent oscillations (shown in Figure S1), the jump from one orientation of another can lead to loss

of intensity of $I_x(CT)$. In analogy to Figure 2A, Figure S5 shows locked $I_x(CT)$ coherence in the absence of motions for C_q values of 10 and 1 MHz at $\omega_0/2\pi = 54.2$ MHz and $5 \cdot 54.2$ MHz. For the case with $C_q = 10$ MHz we observe that, due to the decrease in the Q2 term for the higher magnetic field strength, the percentage of the transverse magnetization in the locked coherences is increased and the overall profile is narrowed. On the other hand, for $C_q = 1$ MHz, the Q2 term is sufficiently reduced for both values of the magnetic field strength, such that the profiles at the two fields almost overlap and, thus, lead to the absence of field dependence for the $R_{1\rho}$ rate in the slow limit for these conditions.

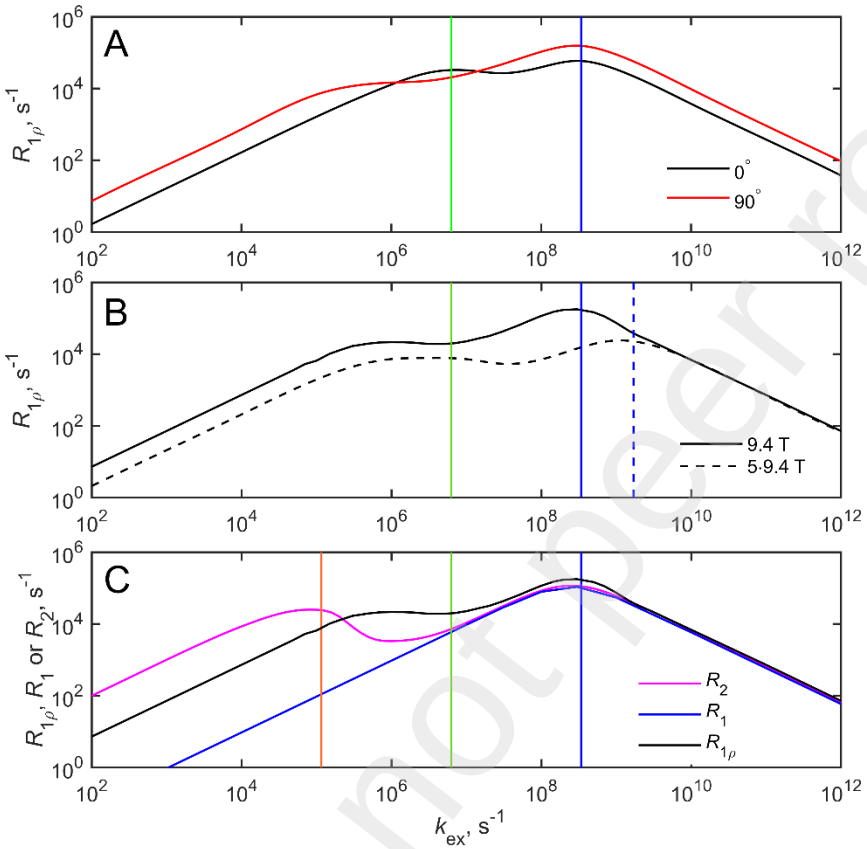

Figure 3. Simulated $R_{1\rho}$, R_1 and R_2 NMR relaxation rates corresponding to the central transition of ^{17}O spin-5/2 system with an axially symmetric EFG tensor with C_q= 10 MHz under the spin-lock field of 35 kHz, as a function of k_{ex} and using the model of the 2-site jumps with the 104.5° jump angle, and under static conditions. A) $R_{1\rho}$ rates for crystallite orientations with the initial principal axis of the quadrupolar tensor aligned either at 0° (black line) or 90° (red line) relative to the static magnetic field of 9.4 T. The vertical solid lines show the values of $\frac{2\pi C_q}{I(2I-1)}$ (green line) or the Larmor frequency ω_0 (blue line). B) Powder-averaged $R_{1\rho}$ rates at two values of the magnetic field strengths, 9.4 (solid line) and 5·9.4 T (dashed line). The additional vertical dashed line stands for the Larmor frequency at 5·9.4T. C) Powder-averaged $R_{1\rho}$ (black line), R_1 (blue line) and R_2(magenta line) rates at 9.4 T magnetic field strength. The additional orange vertical line corresponds to $\frac{1}{\omega_0}\left(\frac{2\pi C_q}{I(2I-1)}\right)^2$. The single exponential approximation was used for all fits of the relaxation rates, which are shown on log scale. 610 crystallite orientations were employed in simulations of the powder-averaged values. The initial conditions are: CT with saturated ST1 and ST2 for $R_{1\rho}$ and R_2; inversion of CT only for R_1 with ST1 and ST2 at equilibrium.

In the fast exchange limit, all three relaxation measurements, R_2, R_1, and $R_{1\rho}$ provide essentially the same information as $R_{1\rho}$ (Figure 3C, $C_q = 10$ MHz). However, in the intermediate and slow regimes the behavior of these rates can be different. The behavior of R_1 is most straightforward and is always dominated by the first order quadrupolar interaction. The $R_{1\rho}$ relaxation undergoes the transition from slow to intermediate regime when the exchange rate is on the order of $\frac{2\pi C_q}{I(2I-1)}$, while for the R_2 rate it is the second order quadrupolar coupling $\frac{1}{\omega_0}\left(\frac{2\pi C_q}{I(2I-1)}\right)^2$ which sets the characteristic scale for the slow to intermediate transition. In the slow limit the values of R_2 are much larger compared to $R_{1\rho}$. Maybe more significantly, because the changes of the relaxation rates in the intermediate regime tend to be less dramatically dependent on the exchange rate than in the slow regime and for R_2 experiment the intermediate region persists to lower valuesof k_{ex}, the $R_{1\rho}$ experiment can be more sensitive to the exchange rates in the range given by $\frac{1}{\omega_0}\left(\frac{2\pi C_q}{I(2I-1)}\right)^2 < k_{ex} < \frac{2\pi C_q}{I(2I-1)}$. The main distinction in the field dependence of R_2 rate, as compared with the $R_{1\rho}$ and R_1 rates, is the absence of the field dependence in the slow motional regime (Figure S6).

Role of initial conditions

Due to the non-exponential nature of the quadrupolar relaxation, the effect of the initial conditions should be considered, as noted in a number of prior works.[12,14,26,27] The apparent ^{17}O CT longitudinal relaxation rates can vary by a factor of 12 for the 2-site jumps model (Figure 4A). For the CT R_1 relaxation the cleanest measurement appears to be the inversion recovery with both ST are at equilibrium, provided that the inversion pulse does not invert ST1. Saturation recovery measurements are more prone to pulse bandwidth consideration, which is further discussed in the experimental section. Methods based on multiple quantum coherences have also been employed to address the non-exponentiality of the longitudinal relaxation.[26] In contrast, ^{17}O CT R_2 rates do not depend on whether the initial conditions for ST is in the saturated or equilibrium sate. However, if ST is in the transverse plan, the R_2 rate is somewhat modified in intermediate regime, but the maximum changes in the rate do not exceed 2.5% for the 2-site jumps model, even when the refocusing pulse acting on the ST coherences is explicitly included, in addition to the CT refocusing pulse.

The situation is somewhat more complex for the CT $R_{1\rho}$ rates. In quadrupolar spin-locking measurements, it is common practice to phase-cycle the preparation and receiver pulses by simultaneously inverting the phases of the excitation pulse and receiver by 180° while keeping the phase of the spin-lock field unchanged, as suggested by Vega and co-workers,[28] to ensure that any additional contributions to the transverse CT magnetization generated during the spin-lock period are eliminated. Otherwise, the longitudinal CT magnetization is created during the spin-lock period itself, which then evolves into the detectable transverse CT magnetization due to the second order quadrupolar interaction. In general, it creates a non-zero equilibrium *transverse* CT magnetization in the presence of the spin-locking field. Note, that an appreciable equilibrium population of the CT arises only in a very specific scenario in which T_1 time is on the order of the $T_{1\rho}$ time and if it is not eliminated by the phase cycle described above. If the phase cycle is not employed, CT $R_{1\rho}$ rates can be sensitive to whether the ST states are in equilibrium or saturated, when the motions are in the intermediate regime (Figure S7). If the ST state(s) are in the transverse plane, the phase cycle is not effective in removing their contributions. In this respect the excitation pulse bandwidth consideration can come into play as well. The maximum changes in $R_{1\rho}$ rates in the intermediate regime

are on the order of 30% for the 2-site jumps model. The effect of ST1 coherence on the $R_{1\rho}$ rate is larger than on the R_2 rate, as the combination of the second order quadrupolar interaction and the spin-locking RF field inter-converts CT and ST1 coherences. The analogous contributions from ST2 are minor and similar in magnitude between the $R_{1\rho}$ and R_2 rates.

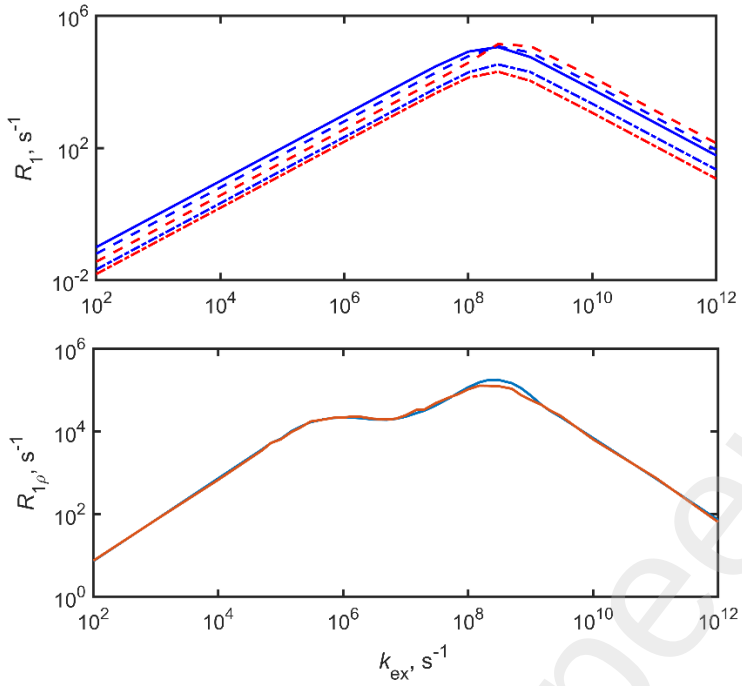

Figure 4. Effect of the initial conditions on the ^{17}O NMR relaxation rates under the 2-site jump model with 104.5° angle. An axially symmetric EFG tensor with C_q = 10 MHz was used and magnetic field of 9.4 T. Relaxation rates on the log scale versus k_{ex}. A) R_1 rates of CT coherences in two versions of experiments: inversion recovery (blue lines) and saturation recovery (red lines) and three types of initial conditions: no saturation of satellite coherences (solid line), saturation of ST1 coherence (dashed lines), and saturation of both ST1 and ST2 coherences (dash-dot line). Solid blue line represents both the IR and SR versions with no saturation of satellite coherences, as these rates coincide. B) $R_{1\rho}$ rates simulated with alternating the phase of the spin-locking field, which removes the contributions from the equilibrium populations of CT and ST. The initial conditions of the excited transverse coherences are: CT only (blue line), CT and ST1 (red line). The spin-lock field strength was 35 kHz. The single exponential approximation was used for all fits of the relaxation rates. 610 crystallite orientations of the static powder were employed.

II. Experimental implementation of ^{17}O NMR relaxation times measurements

In the weak field limit when $\omega_{RF} \ll \frac{2\pi C_q}{I(2I-1)}$, the central transition nutates with the frequency of $3\omega_{RF}$.[29] Thus, the maximum excitation is achieved with the 30° pulse,[16,29] while the inversion or refocusing can be accomplished with the 60° pulse. If a pure excitation of the CT transition is desired, the excitation pulse has to be selective enough to exclude all crystallites of the first satellite transition. The pulse bandwidth can be estimated by the expression $2.8/\pi\tau_p$, where τ_p is the pulse length.[12] A saturated state of the ST1 can be achieved using selective off-resonance irradiation centered at the ST1. We used the sequence consisting of 10 pairs of Gaussian pulses with alternating positive and negative offsets (10 μs duration for a pair of Gaussian pulses with ±300 kHz offset), spaced at 1 μs intervals (Figure 5). This sequence, referred to as

"RAPT", [30] was optimized for the saturation of ST and enhancement of the CT in the presence of MAS but can also be employed in the case of static solids. The method is an extension of the earlier work by Haase et al.[27] on manipulation of population transfers in quadrupolar nuclei of static solids using frequency swept RF fields.

The detection scheme for the wide powder pattern of ^{17}O nuclei with the relatively low value of the gyromagnetic ratio needs to consider minimization of acoustical ringing effects. This can be achieved either by the traditional Hahn echo scheme, [31] or the recently developed TRIP sequence, [32] consisting of three phase-cycled 30° pulses. The former scheme decreases signal intensity due to T_2 losses.

The CT line shapes were collected using the Hahn echo pulse sequence ($\tau_p - \Delta - 2\cdot\tau_p - \Delta$) with the echo delay Δ = 25 μs and τ_p = 2 μs at 41.7 kHz RF field, yielding 450 kHz excitation bandwidth. The spectral window was 400 kHz at temperatures above 245 K and 800 kHz at 235 K and below. The partial excitation of the ST1 enters into the line shapes as a raised baseline.

At several temperatures the line shapes were also taken with the TRIP pulse sequence and inclusion of the RAPT block. The CT line shapes collected with the TRIP scheme were similar in shape to those obtained with the echo collection method at higher temperatures up to about 215 K. However, at lower temperatures (Figure S8), the TRIP resulted in a distorted line shape due to the receiver deadtime, which was compensated in the refocusing delay in the echo method. Thus, for consistency all line shapes presented in Figure 6 are those collected with the Hahn echo scheme.

As elaborated in the "Theoretical and computational description of the ^{17}O NMR relaxation in powders" section and in Figure 4, the choice of initial conditions in general affects the resulting relaxation times. The RAPT block preceding excitation of the transverse coherence helps in establishing a purer CT excitation, with less dependence on the excitation bandwidth. For the longitudinal coherence, the inversion recovery sequence without pre-saturation of ST1 is expected to yield the most accurate relaxation times measurements, which are least dependent on the extent of inversion and pre-saturation of ST1. In the slow motional regime, it is also expected to yield the shortest T_1 values. We, thus, choose it as our main approach for the temperature-dependence collection of T_1 times. At selected temperature points we also conduct a version of the T_1 saturation recovery measurements for T_1 times measurements to probe the theoretical expectations in regard to the dependence of the relaxation times on the initial conditions. Pulse imperfection and bandwidth consideration can also be included directly into the simulations routine when needed.

T_2 relaxation times were measured with the Hahn echo pulse sequence preceded by the RAPT block (RAPT–τ_p–τ_D/2–2·τ_p–τ_D/2) with τ_p = 2 μs (corresponding to 30° pulse at 41.7 kHz RF field) and a variable relaxation delay τ_D. T_1 times across the entire temperature range were obtained using the inversion recovery scheme (2·τ_p – τ_D – detect) with τ_p = 2 μs as above. The detection scheme was chosen as TRIP to avoid T_2-related intensity losses. The measurements were repeated at two low temperatures with the echo detection scheme to confirm the results.

Rotating frame relaxation must involve a spin-locking field of sufficient strength to lock the desired interaction. For the central transition of the ^{17}O nuclei the most efficient locking is expected for the spin-locking field strength of about 30 kHz (Figure S9, shown for 14.1 T, C_q =12.5 MHz and η = 0.8). The locking efficiency is diminished for smaller values of the spin-locking field strengths below about 15 kHz, for which the second order quadrupolar interaction provides an effective exchange with coherences other

than transverse magnetization. The locking efficiency then becomes optimal in the 25 to 60 kHz range, and slowly diminishes for much higher spin-locking fields due to introduction of non-central transitions into the locked transverse coherence. We employed spin-lock field strength of 35 kHz, applied "on-resonance", approximately in the middle of the CT line at 283 ppm for all temperatures. The phase cycle of Vega and coworkers was employed,[28] implemented by alternating the phases of the excitation pulse and the receiver simultaneously by 180°. Another potential modification of the $T_{1\rho}$ experiment can include the heat compensation block to account for the differences in RF-induced heating as a function of the variable relaxation delay.[33] In the case of $NaNO_3$ it was not needed, but can become important if the method is applied to hydrated and/or biological samples. The main pulse sequence employed for the collection of the temperature-dependence $T_{1\rho}$ times is shown in Figure 5. It involves saturation of ST1 for the suppression of the residual ST1 transverse magnetization using the RAPT block, and τ_p = 2 μs excitation pulse at 41.7 kHz RF field. The omission of the RAPT block is expected to have an effect only in the intermediate motional regimes (refer to Figure 4B in the "Theoretical and computational description of the ^{17}O NMR relaxation in powders" section). The detection immediately preceded the spin-lock period except for the lowest temperature, in which significant spectral distortions necessitated the use of the echo detection scheme. At several temperatures we also measured $T_{1\rho}$ times without the saturation of ST1, in which case the RAPT block was omitted, and a more selective excitation was achieved with τ_p = 5 μs excitation pulse at 16.7 kHz RF field.

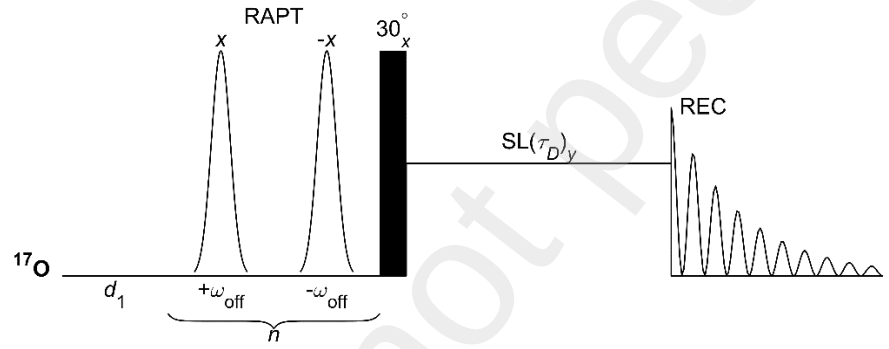

Figure 5. The pulse sequence for measurements of ^{17}O NMR CT $T_{1\rho}$ relaxation times: after the inter-scan delay d_1, the (optional) RAPT suppression of satellite transitions consisting of loops of off-resonance Gaussian pulses[30] applied at the offsets of ±300 kHz is employed, followed by the 30° excitation pulse (2 μs at 41.7 kHz), and then by the spin-lock period of the variable delay SL(τ_D), applied at the center of the spectrum (on-resonance) with the RF field amplitude of 35 kHz. The FID collection immediately proceeds the spin-lock period. The phase cycle of Vega et al. is employed. [28]

III. Relaxation times and line shapes in the 280 to 195 K temperature range.

The relaxation times and line shapes (Figures 6-8) were measured in the 280 to 195 K temperature range at 14.1 T. The limits of the range were defined by the limits of feasibility of the $T_{1\rho}$ magnitudes measurement. $T_{1\rho}$ times lie between 9 μs and 5.5 ms in this temperature range. Above 280 K $T_{1\rho}$ relaxation times are expected to be too short to be measured reliably, and below 195 K they are expected to be too long and would require relaxation delay times beyond the RF limit of the probe, which was about 20-25 ms on our probe for the spin-lock field of 35 kHz. The single-exponential approximation was adequate to fit all of magnetization decay/build up curves. The fit utilized the version with the baseline, $M(t) = M_0 e^{-t/T_{1\rho}} + B$.

The presence of baseline is due to inherently non-exponential nature of relaxation in solid state, as elaborated in the "Theoretical and computational description of the ^{17}O NMR relaxation in powders" section. Contributions from the orientations for which the decay is very slow cannot be reliably included in the overall single exponential decay fit, but could manifest themselves as a baseline. These contributions didn't exceed 10%. The resulting relaxation times are shown in Figure 8.

The temperature dependence of T_1 clearly shows that it is in the slow regime with respect to the Larmor frequency, while the inflection in the temperature dependence of $T_{1\rho}$ indicates the slow regime approaching the intermediate regime, as defined by $\frac{2\pi C_q}{I(2I-1)} = 7.9 \cdot 10^6\ \mathrm{s}^{-1}$. Non-monotonic temperature dependence of T_2 times with temperature indicates that the motions span slow and intermediate regimes. The lower limit of the intermediate regime for the T_2 experiment is defined by $\frac{1}{\omega_0}\left(\frac{2\pi C_q}{I(2I-1)}\right)^2 = 1.2 \cdot 10^5\ \mathrm{s}^{-1}$.

To check the effect of carrier position on $T_{1\rho}$ times we have performed additional measurements at 205 K and 245 K with the carrier position shifted by 421 ppm downfield (centered on the left peak), as compared to the main series taken with the carrier placed at 283 ppm. There was no difference in the resulting $T_{1\rho}$ times within experimental errors.

To probe the dependence of T_1 times on the initial conditions, we have also performed the saturation recovery version of the measurements for 265, 225, 205, and 195 K utilizing the RAPT block and a loop of 30° pulses (2 μs at 41.47 kHz RF field strength) as the saturation components. The combination of the RAPT block and the relatively wide bandwidth pulse of 2 μs (corresponding to the bandwidth of 445 kHz) is aimed to maximize the saturation of both ST1 and CT. Based on the 3-site jump model, the expected theoretical factor in the increase of T_1 times between the inversion recovery of the CT and the saturation recovery is 3.4 in the slow limit, while the experimental factor is 2.8-3.1 for all cases. The most likely cause of the discrepancy is incomplete saturation of ST1 in the experiment. Nonetheless, the measurements clearly demonstrate the importance of taking into account the initial conditions for the T_1 times measurements. For $T_{1\rho}$ measurements in the slow regime and at the approach to the intermediate regime we do not expect difference between $T_{1\rho}$ times with and without ST1 saturation when the phase cycle of Vega and coworkers [28] is employed (Figure 4B). To check whether this holds for the experimental data we have performed a different version of the $T_{1\rho}$ measurements at 280, 225, and 205 K, during which we omitted the RAPT block and employed a more selective excitation with τ_p = 5 μs excitation pulse at 16.7 kHz RF field. No difference in $T_{1\rho}$ times was detected within the experimental errors.

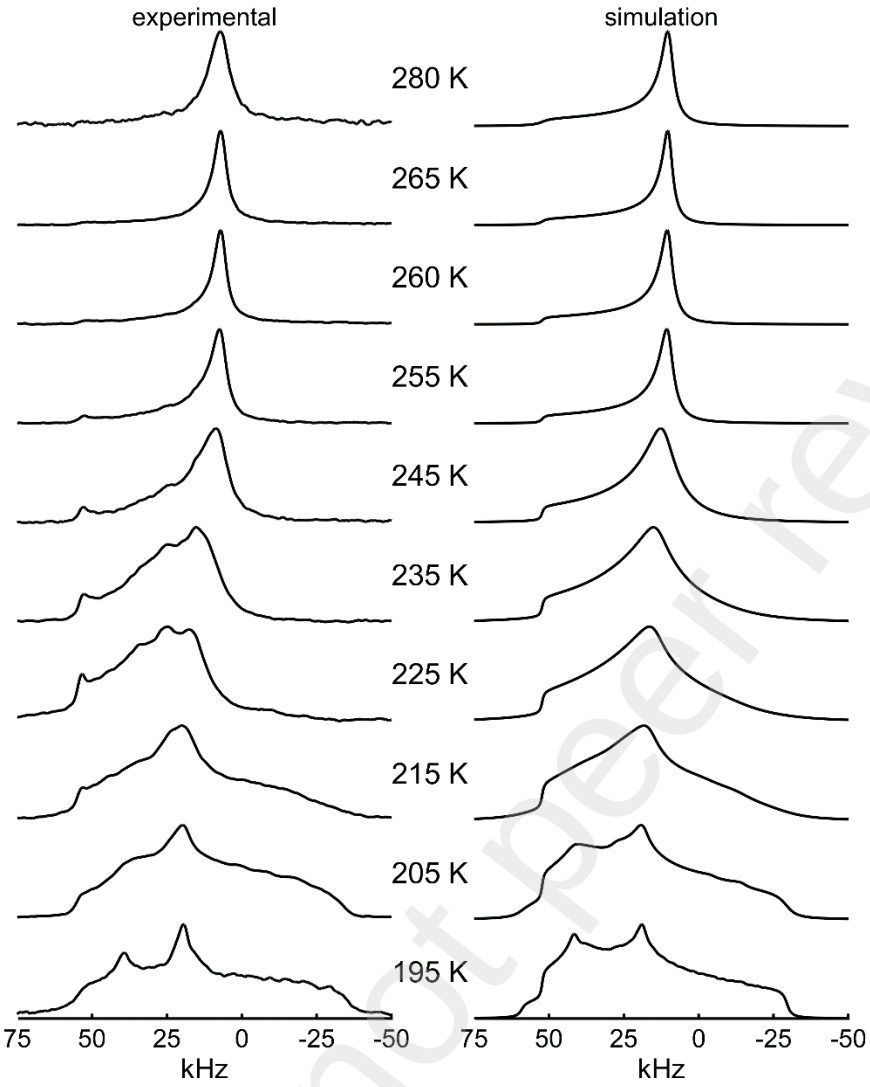

Figure 6. Normalized experimental (left) and simulated (right) ^{17}O line shapes of $NaNO_3$ at 14.1 T under static conditions. The Hahn echo detection scheme with the 25 μs delay was used. Simulations included explicit 3-fold jumps of the NO_3^- group using the tensor parameters described in the text and demonstrated in Figure 1.

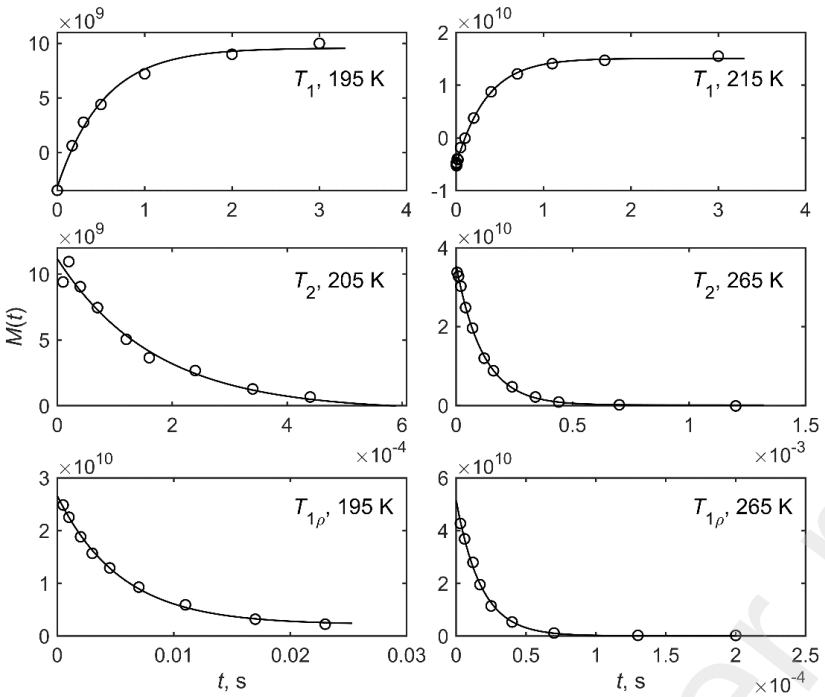

Figure 7. Examples of magnetization decay and build up curves $M(t)$ for the ^{17}O T_1 (first row), T_2 (second row) and $T_{1\rho}$ (third row) relaxation times of $NaNO_3$ at 14.1 T. $M(t)$ in arbitrary units versus the relaxation time t. The temperatures are shown directly on the panels. The monoexponential fits to $M(t) = M_0 e^{-t/T_{1\rho}} + B$ are shown as lines.

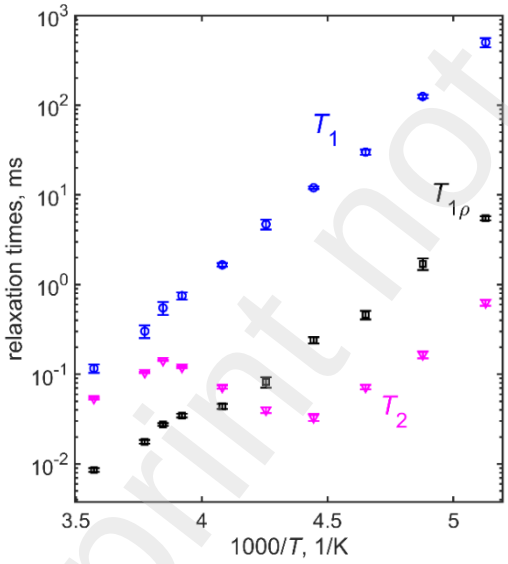

Figure 8. Semilog plots of the ^{17}O NMR relaxation times T_1 (blue circles), $T_{1\rho}$ (black circles) at 35 kHz spin-locking field, T_2 (magenta triangles) versus $1000/T$ collected for $NaNO_3$ at 14.4 T using the single-exponential fits. The experimental schemes are the following: T_1- inversion recovery of CT line with 4 μs pulse at 41.7 kHz RF, $T_{1\rho}$ - using of the pulse sequence of Figure 5, the spin-lock field of 35 kHz, presaturation of ST1, and 2 μs excitation pulse at 41.7 kHz RF, T_2 Hahn echo with the presaturation of ST1 and and 2 μs excitation pulse at 41.7 kHz RF.

IV. Comparison of the rate constants obtained from ^{17}O relaxation and line shapes measurements

We used the quadrupolar and CSA tensor parameters reported in Hung et al.[9], $C_q = 12.5$ MHz, $\eta = 0.8$ for the EFG tensor and [δ_{11}, δ_{22}, δ_{33}] = [250 400 550] ppm for the CSA tensor, with relative orientation [0, 90°, 90°] of the two PAS frames. The definition of the tensor components and their relative orientations are shown in Figure 1. Homonuclear dipolar couplings between ^{17}O nuclei are ignored due to the much smaller ^{17}O-^{17}O dipolar coupling constant (on the order of 60 Hz for a pair of intramolecular oxygens in $NaNO_3$). Additionally, the degree of ^{17}O isotopic incorporation was measured by Beewerth et al. using the same preparation protocol to be 4.5%, [20] thus rendering intra-molecular ^{17}O-^{17}O coupling a low occurrence.

The line shapes are consistent with the previously determined tensor parameters and yield the values of k_{ex} shown in Figure 9 and the temperature-dependent isotropic chemical shift in Figure S10. There is no perfect fit of all features between the experiment and the simulations, probably due to effect of experimental imperfections such as excitation bandwidth consideration,[20] etc. In general, the sensitivity of line shapes to the value of k_{ex} appears to be lower than the ones resulting from the relaxation rates, and we state the values corresponding to the best visual comparison without the estimate of error bars.

The fits of k_{ex} values to the experimental relaxation rates were performed using simulations procedure stated in the Materials and Methods section, taking care to use simulated values of relaxations delay times τ_D identical to those in the experiment to avoid skewing the simulated data due to the inherent non-exponentiality of relaxation. Due to non-monotonic dependence of T_2 on k_{ex} in the experimental region, the fits of T_2 times were constrained to yield k_{ex} values that decrease with temperature. For two temperatures, this was not enough to resolve the ambiguity of the fitted k_{ex} values, and it had to be resolved on the basis of the values obtained from the T_1 and $T_{1\rho}$ fits. The results are demonstrated in Figure 9. The errors in the resulting k_{ex} values were determined by propagation of the experimental errors in the relaxation times. There is a good overall agreement between all fitted k_{ex} values obtained from all measurements. The values of the Arrhenius activation energies E_a obtained from each of the series separately (T_1 : E_a = 44.4 ± 0.5 kJ/mol, $T_{1\rho}$: E_a = 47 ± 2 kJ/mol, T_2 : E_a = 49 ± 3 kJ/mol, line shape: E_a = 41 ± 2 kJ/mol) are also in a reasonable agreement with each other as well with the value obtained from the line shape measurement by Hung at el., 44.5 ± 2 kJ/mol, when the same temperature range of 280 to 195 K is taken for their 14.1 T data set. The weighted average of E_a obtained from the individual data set is 44.4 ±0.5 kJ/mol.

An additional confirmation of the results of k_{ex} values can be obtained by comparing their consistency with the expected results at a different value of the magnetic field. Experimental T_1 and $T_{1\rho}$ relaxation times obtained at 18.8 T in the 265 to 200 K range (Figure S11) are in good agreement with the prediction based on rate constants originating from the 14.1 T relaxation times.

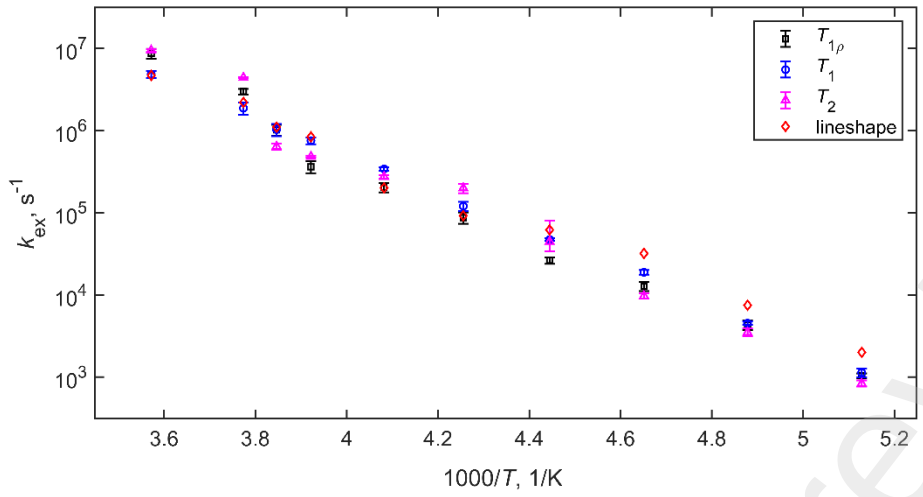

Figure 9. Fitted values of k_{ex} versus $1000/T$ from all of the ^{17}O T_1, T_2, $T_{1\rho}$ relaxation and line shapes measurements in $NaNO_3$ at 14.1 T.

The combined approach of using multiple ^{17}O NMR relaxation times and line shapes allows for a better control of issues such as the dependence of the rates on the initial conditions, pulse bandwidth considerations, different sensitivity to motional regimes with respect to the Q1 and Q2 terms. While the T_1 experiment has a single well-defined minimum centered on the Larmor frequency, it is most sensitive to the effect of the initial conditions across the entire dynamics range and can be thus dependent on pulse bandwidth considerations. The T_2 experiment on the other hand is least sensitive to the initial conditions but has two broad minima given by $\frac{1}{\omega_0}\left(\frac{2\pi C_q}{I(2I-1)}\right)^2$ and by the Larmor frequency, which may complicate an unambiguous determination of the rate constants if used in isolation. The $T_{1\rho}$ experiments appears to be a good compromise between the minimal dependence on the initial conditions (when the appropriate phase cycle and RAPT scheme are used) and the widths of the intermediate regimes region, given by $\frac{2\pi C_q}{I(2I-1)} < k_{ex} < \omega_0$. The line shapes are very sensitive to the quadrupolar and CSA parameters, but can be less sensitive to the k_{ex} values, as discussed above. A possible extension of the experimental approach can involve the use of Gaussian pulses for enhancing the selectivity of the excitation or inversion of the central line.

In the case of $NaNO_3$ the multiple measurements may appear somewhat redundant, however they demonstrate the application of the combined approach to more complex systems with multiple motional modes and unknown tensor parameters. In this case, several relaxation rates may distinguish the details of the multi-modal mechanisms on different time scales and provide a more precise determination of the corresponding rate constant and populations of conformational states.

Materials and Methods

The $NaNO_3$ sample in the crystalline phase was generously provided by Gang Wu and prepared as described in reference [9].

I. NMR measurements

The measurements were performed using the 14.1 T and 18.8 T spectrometers at Maglab, equipped with the static low E probe of 5 mm coil diameter.[34] The temperature was calibrated using lead nitrate. Cooling was achieved with liquid nitrogen. The number of scans varied between 8 and 32 in the relaxation times measurements and 32 to 128 in the line shape measurements. The inter-scan delay was 1-2 s. 4 to 8 dummy scans were employed in the relaxation measurements. Other experimental parameters and schemes are stated in the Results and Discussion section.

II. Simulations

Modeling of a relaxation experiment involves setting up initial coherence, simulating the evolution during mixing period, and generating the detected signal in the form of free induction decay. For the line shape simulation the mixing period step is omitted.

The idealized initial conditions take into account non-zero equilibrium values of the coherences unaffected by the preparatory pulses. For example, for the T_1 inversion-recovery CT simulation the initial coherence is $\rho(0) = -I_z(CT) + I_z(ST1) + I_z(ST2)$, for the inversion-recovery CT with saturated ST1 it is $\rho(0) = -I_z(CT) + I_z(ST2)$, and for the saturation recovery with CT and ST1 saturated $\rho(0) = I_z(ST2)$. For the $T_{1\rho}$ and T_2 simulations with only CT excitation $\rho(0) = I_x(CT) + I_z(ST1) + I_z(ST2)$, etc. The equivalent of the phase cycling necessary for $T_{1\rho}$ simulations was implemented through alternating the sign of the RF term in the Liouvillian. The equilibrium magnetization was taken as $\rho^0 = I_z(CT) + I_z(ST1) + I_z(ST2)$ in all simulations.

Evolution during the mixing period was simulated by solving the differential equations Eq. (5) by matrix exponentiation using the internal Matlab algorithm.[35,36] The full set of 35 spin 5/2 coherences was used to represent the density matrix for a single orientation, Eqs. (S1) and (S2), supplemented by an extra state to maintain the equilibrium magnetization. Because there are three possible orientations for N–O bond in the NO_3^- ion, the overall size of $\rho_{j,m}$ vector is 108 components. The three orientations of the N–O bond vector in a single crystallite have equal occupation numbers, which is reflected in the symmetric exchange matrix

$$K = k_{ex}\begin{pmatrix} -2 & 1 & 1 \\ 1 & -2 & 1 \\ 1 & 1 & -2 \end{pmatrix}.$$

The orientation-dependent parameters of CSA and EFG tensors were converted through a sequence of transformations starting with the CSA PAS frame into the EFG PAS frame to the molecular frame (with *z*-axis directed perpendicular to the NO_3^- plane and the N–O bond orientations at 0°, 120° and 240°) and, finally, into the laboratory frame for individual crystallites using the corresponding Wigner matrices. The set up of motional frames, as well as the steps of the transformation of the tensors between different coordinate systems were taken from the EXPRESS program written by Vold and Hoatson.[37]

Relaxation arising from the stochastic fluctuations of the CSA tensor and the secular parts of the EFG tensors is accounted for by the explicit Liouvillian term through the exchange between different N–O bond orientations. Non-secular CSA terms were not included due to their negligible contributions. Relaxation due to non-secular quadrupolar interaction terms oscillating at the Larmor and twice Larmor frequencies

are included in the Redfield approximation. Following the approach of the EXPRESS program,[37] we calculate the relaxation matrices in the Redfield approximation entering Eq. (5) as

$$R_{ij} = R_{ij}^1 + R_{ij}^2 \quad (6)$$

with $R_{ij}^M = \sum_\alpha \frac{V_{M,\alpha} V_{-M,\alpha}^* \lambda_\alpha}{\lambda_\alpha^2 + M^2\omega_0^2} C_{ij}^M$. Here, λ_α are non-zero eigenvalues of the exchange matrix K, $V_{M,\alpha}$ are the projections of the components of the quadrupolar tensor on the eigenvectors corresponding to non-zero eigenvalues λ_α, and C_{ij}^M are commutators of the second order spherical operators corresponding to the fast-oscillating quadrupolar interaction terms.

For the simulations of the T_2 experiment, the evolution during the mixing period was split into two halves with the 180° refocusing pulse in between the two. Relaxation delay times used in the simulations for the fits of the experimental data were matched with those employed in the experiment.

Following the evolution period, the detection block can be implemented explicitly: for the inversion or saturation recovery T_1 experiment, $I_z(CT)$ coherence was transformed into the transverse plane, while for the T_2 and the $T_{1\rho}$ simulations no additional transformations were applied before the acquisition period. However, it is possible to include other detection schemes such as the Hahn echo. The inclusion of Hahn echo block did not change the outcomes of the simulated relaxation times or line shapes.

The acquisition block included a single component of the I_- operator corresponding to the central transition, with the details of the approach specified in the SI2. This reduced the 36-component coherence vector for a single site in the 3-fold jumps model down to a single coherence. The size of the Liouvillian matrix is reduced accordingly. Nonetheless, the relaxation during the acquisition period can still be taken into account, including the Redfield terms in Eq. (6) in addition to the Liouvillian terms. This procedure is clarified and extended from the approach presented in [37]. The propagation matrix is calculated by exponentiation of the reduced Liouvillian matrix multiplied by the dwell time. The reduced coherence vector is then repeatedly multiplied by this propagation matrix. Finally, the free induction decay curve is obtained by adding the resulting coherences for all sites.

The powder averaged spectra as well as magnetization decay and build up curves in the relaxation measurements require averaging over the crystallite orientations. The choice of the number of discreet orientations included in the averaging is dictated by the stability of the fitted relaxation times and jitter-free line shapes. We found the commonly used ZCW scheme[38,39] adequate based on our tests. For the relaxation times simulations, the 610-orientations grid was chosen. It yields the results differing from the smaller 377-orientations grid by no more than 1%. For the line shape simulations, the 17711-orientations grid was sufficient. The latter grid was also used to produce the orientation-dependent (rather than powder averaged) relaxation rates reported in the "Theoretical and computational description of the ^{17}O NMR relaxation in powders" section.

Simulations of relaxation took about 3 minutes for one magnetization decay curve with 11 relaxation delays using the 610-orientations crystallite averaging and the 3-site jump model on Intel Core i7 2.60 GHz CPU with an ordinary laptop, and about 5 minutes for the 17711-orientations crystallite averaging for the line

shapes simulations. The calculation times can be reduced by an order of magnitude if parallel processing for different crystallites is used on a dedicated CPU of the same type.

Conclusion

This work explored the combined approach using multiple ^{17}O CT NMR relaxation times ($T_{1\rho}$, T_1, and T_2) as well as CT line shape analysis to enhance the tools for studies of molecular dynamics. Each method in isolation has its own limitations, broadly defined by the sensitivity to the initial conditions on one hand, the potential ambiguities and complex behavior around the intermediate regime on the other hand, the general sensitivity to the motional parameters for the relevant temperature ranges, and experimental limitations on the magnitudes of the relaxation times that can be measured.

We used $NaNO_3$ as a model compound under static (non-spinning) conditions to probe experimental limitations of each method in isolation. We included modelling of the relaxation experiments for an arbitrary system undergoing large-angle 2-site jumps to explore theoretical limitations and establish the modeling routines. The T_1 times have a single minimum with respect to dependence on the rate constant, however they are the most dependent on the initial conditions. The T_2 times are the least dependent on the initial conditions but have a rather complex dependence on the rate constant in the broad intermediate motional regime, which can create ambiguities if these measurements are used in isolation. The novel $T_{1\rho}$ experiment is shown to have a minimal dependence on the initial conditions (when the appropriate phase cycle is employed) and a narrower width of the intermediate regime region compared with the T_2 measurements. However, it requires the employment of the spin-locking field strong enough to lock the CT line, which invokes probe RF limits considerations, especially for long $T_{1\rho}$ times. The line shape measurements can have a limited sensitivity to the rate constant outside of the intermediate regimes but are the simplest to perform and model. They provide direct information about quadrupolar and CSA tensor parameters.

In general, the Redfield approach may not be valid across the entire range of temperatures for the R_2 and $R_{1\rho}$ relaxation rates and, thus, the numerical solutions to the Liouville – von Newman equation remains the most general tool. We develop the protocols for simulations of the relaxation rates and line shapes of half-integer quadrupolar nuclei with the explicit inclusion of the motional model into the routine.

For the model compound of $NaNO_3$, we have implemented this numerical approach to fit the rate constants of the 3-fold jumps obtained on the basis of line shapes, T_1, T_2, and $T_{1\rho}$ relaxation times measurements in the 280 to 195 K temperature range. The temperature range was governed by the limits of sensitivity for the $T_{1\rho}$ measurements, which is determined on the fast side by the length of the relaxation times that are still feasible to detect experimentally (above 8-10 μs) and on the low side by limitation of the RF-induced probe heating, which corresponded to feasibility of measurements for $T_{1\rho}$ times below about 10 ms in our case. A reasonable agreement in the resulting values of rate constants was obtained from all the measurements, and we discussed the complementarity of all the measurements to raise the accuracy of the resulting value of the activation energy.

The combined approach is expected to be especially useful for complex systems with unknown motional models and tensor parameters, and the ^{17}O $T_{1\rho}$ measurements constitute an important addition to the suite of the relaxation experiments in this regard. While the approach is presented here for static powders, it is

extendable to rotating solids, for which the evolution under magic-angle spinning should be carefully taken into account in simulations, and the potential for rotary resonances considered in the choice of experimental parameters for the $T_{1\rho}$ measurements.[40,41] Magic-angle spinning will also reduce the contributions to non-exponentiality related to orientation-dependent relaxation rates.

Acknowledgements

Experiments were performed at the National High Magnetic Field Laboratory, which is supported by NSF Cooperative Agreement NSF/DMR-2128556, the State of Florida, and the U.S. Department of Energy. A part of this work was supported by the National Institutes of Health grant R15-GM111681 to L.V.

References

[1] S.E. Ashbrook, Z.H. Davis, R.E. Morris, and C.M. Rice, Chem. Sci. 12 (2021) 5016-5036.
[2] G. Wu, Prog. Nucl. Magn. Reson. Spec. 114-115 (2019) 135-191.
[3] I.P. Gerothanassis, Prog. Nucl. Magn. Reson. Spectrosc. 56 (2010) 95-197.
[4] E.G. Keeler, V.K. Michaelis, C.B. Wilson, I. Hung, X. Wang, Z. Gan, and R.G. Griffin, J. Phys. Chem. B 123 (2019) 3061-3067.
[5] V. Lemaître, M.E. Smith, and A. Watts, Solid State Nucl. Magn. Reson. 26 (2004) 215-235.
[6] I. Hung, E.G. Keeler, W. Mao, P.L. Gor'kov, R.G. Griffin, and Z. Gan, J. Phys. Chem. Lett. 13 (2022) 6549-6558.
[7] S. Muniyappan, Y. Lin, Y.H. Lee, and J.H. Kim, Biology 10 (2021).
[8] I. Goldberga, N. Patris, C.-H. Chen, E. Thomassot, J. Trébosc, I. Hung, Z. Gan, D. Berthomieu, T.-X. Métro, C. Bonhomme, C. Gervais, and D. Laurencin, J. Phys. Chem. C 126 (2022) 12044-12059.
[9] I. Hung, G. Wu, and Z. Gan, Solid State Nucl. Magn. Reson. 84 (2017) 14-19.
[10] E.G. Keeler, V.K. Michaelis, and R.G. Griffin, J. Phys. Chem. B 120 (2016) 7851-7858.
[11] J. Beerwerth, M. Storek, D. Greim, J. Lueg, R. Siegel, B. Cetinkaya, W. Hiller, H. Zimmermann, J. Senker, and R. Böhmer, J. Magn. Reson. 288 (2018) 84-94.
[12] A.C.N.J.F. Bunn, D.;Haase, J., NMR Basic Principles and Progress:Special Applications, Springer Berlin, Heidelberg, Heidelberg 1993, pp. 1-178.
[13] A. Abragam, Principles of Nuclear Magnetism, Clarendon Press, Oxford, 1961.
[14] J. Haase, K.D. Park, K. Guo, H.K.C. Timken, and E. Oldfield, J. Phys. Chem. 95 (1991) 6996-7002.
[15] S.E. Ashbrook, and S. Wimperis, J. Chem. Phys. 120 (2004) 2719-31.
[16] S.E. Ashbrook, and S. Wimperis, J. Chem. Phys. 131 (2009) 194509.
[17] L. Werbelow, and G. Pouzard, J. Phys. Chem. 85 (1981) 3887-3891.
[18] R. Janssen, and W.S. Veeman, J. Chem. Soc., Faraday Trans. 84 (1988) 3747-3759.
[19] H.J. Hogben, M. Krzystyniak, G.T.P. Charnock, P.J. Hore, and I. Kuprov, J. Magn. Reson. 208 (2011) 179-194.
[20] J. Beerwerth, R. Siegel, L. Hoffmann, L.S. Plaga, M. Storek, B. Bojer, J. Senker, W. Hiller, and R. Böhmer, Appl. Magn. Reson. 51 (2020) 597-620.
[21] P.P. Man, Quadrupolar Interactions, eMagRes, 2011.
[22] L. Vugmeyster, and D. Ostrovsky, Chemphyschem. 20 (2019) 333-342.
[23] G.J. Bowden, and W.D. Hutchison, J. Magn. Reson. 67 (1986) 403-414.
[24] T.E. Bull, S. Forsén, and D.L. Turner, J. Chem. Phys. 70 (1979) 3106-3111.
[25] P.S. Hubbard, J. Chem. Phys. 53 (1970) 985-987.
[26] S. Wimperis, G.E. Rudman, and K.E. Johnston, J. Phys. Chem. C 128 (2024) 5453-5460.
[27] J. Haase, M.S. Conradi, C.P. Grey, and A.J. Vega, J. Magn. Reson. A 109 (1994) 90-97.
[28] A.J. Vega, J. Magn. Reson. 96 (1992) 50-68.
[29] W.S. Veeman, Z. Naturforsch. A 47 (1992) 353-360.
[30] Z. Yao, H.-T. Kwak, D. Sakellariou, L. Emsley, and P.J. Grandinetti, Chem. Phys. Lett .327 (2000) 85-90.

[31] E.L. Hahn, Phys. Rev. 80 (1950) 580-594.
[32] F. Wang, S.K. Ramakrishna, P. Sun, and R. Fu, J Magn Reson 332 (2021) 107067.
[33] A.G. Palmer, C.D. Kroenke, and J.P. Loria, Methods Enzymol. 339 (2001) 204-238.
[34] P.L. Gor'kov, E.Y. Chekmenev, C. Li, M. Cotten, J.J. Buffy, N.J. Traaseth, G. Veglia, and W.W. Brey, J. Magn. Reson. 185 (2007) 77-93.
[35] A.H. Al-Mohy, and N.J. Higham, SIAM J. Matrix Anal. Appl. 31 (2010) 970-989.
[36] N.J. Higham, SIAM J. Matrix Anal. Appl. 26 (2005) 1179-1193.
[37] R.L. Vold, and G.L. Hoatson, J. Magn. Reson. 198 (2009) 57-72.
[38] S.K. Zaremba, Ann. di Mat. Pura ed Appl. 73 (1966) 293-317.
[39] V.B. Cheng, H.H. Suzukawa, and M. Wolfsberg, J. Chem. Phys. 59 (1973) 3992-3999.
[40] P. Schanda, J Magn Reson 306 (2019) 180-186.
[41] L. Vugmeyster, D. Ostrovsky, A. Greenwood, and R. Fu, J. Magn. Reson. 337 (2022) 107171.